InSAR Time Series Analysis to Evaluate Subsidence Risk of Monumental Chandigarh City (India) and Surroundings

Jungrack Kim, Shih-Yuan Lin, Tejpal Singh, and Ramesh P. Singh, *Senior Member, IEEE*

***Abstract*— Groundwater depletion is one of the serious geoenvironmental issues causing ground subsidence, which damages buildings, infrastructures, and causes loss of life. The quantitative and qualitative evaluation of groundwater variability requires multiple approaches to measure hydraulic head level and geodetic deformation. In this study, we have made efforts to integrate multiple hierarchical space-borne data, including Gravity Recovery and Climate Experiment (GRACE), Sentinel-1 interferometric synthetic aperture radar (InSAR), and geological and hydrological data, to quantify subsidence in Chandigarh city and its surroundings. First, we conducted New-Small BAseline Subsets (NSBASs) and pointwise persistent scatterer (PS) InSAR techniques in parallel, using three-year Sentinel-1 data showing a vertical subsidence up to 120 mm/year around fluvial sediment deposits. Furthermore, correlation analysis of hydraulic/climatic measurements clearly shows the subsidence associated with the groundwater depletion. The pattern of PS points shows the instability of structures associated with the ground subsidence over the central city areas. The monumental architectures designed by Le Corbusier in the northern sectors are outside of the main subsidence area. In the target area, the magnitude of subsidence and surface deformation due to groundwater depletion depends on the subsurface geophysical environment and the anthropogenic activities within the region and surroundings. The results provided a case of monitoring scheme using multiresolution satellite data about the subsidence and associated consequences due to groundwater depletion.**

***Index Terms*— Groundwater depletion, interferometric synthetic aperture radar (InSAR), risk assessment, subsidence, time series analysis.**

I. Introduction

GROUNDWATER is one of the main natural resources governing human civilization during the industrialization of developing countries. It is primarily used to sustain growing population pressure and agricultural productivity need in developing countries such as India. However, increasing consumption of groundwater for drinking, industry, and irrigation without recharge can cause serious water problems, such as water quality, increased salinity, ground subsidence, and even earthquakes [1], [2], [3]. Among these problems, ground subsidence is a slow deformation associated with the loss of groundwater that causes widespread structural instability in human settlements in many megacities [4], [5], [6] and water basins [7], [8], [9]. Detecting and monitoring the slow deformation associated with groundwater depletion will help the authorities to take appropriate measures to minimize the risk of subsidence.

Ground subsidence due to groundwater withdrawal and depletion has been estimated using numerical modeling, and various approaches to predict subsidence in vulnerable areas, including aquitard drainage [10], poroelasticity [11], and poroviscosity [12], and semiempirical/empirical models [13], [14]. Such efforts enable the implementation of modeling through software tools; for instance, modular three-dimensional finite-difference ground-water flow model (MODFLOW)-interbed storage package (IBS). However, as available initial conditions, such as hydraulic pressures, porosity, and storability of the target area, are only occasionally available, it is difficult to predict the propagation of ground subsidence by groundwater depletion using numerical modeling alone. Also, in situ monitoring using GPS and water levels needs to establish a data network with sufficient spatiotemporal density. Therefore, interferometric synthetic aperture radar (InSAR) has been used as a powerful method to detect and monitor ground subsidence induced by groundwater depletion as reviewed by Galloway and Hoffmann [15]. In several cases, InSAR successfully investigated ground subsidence by groundwater depletion [16], [17], [18], especially with the development of time series analysis techniques that enable the continuous monitoring of ground subsidence.

In this study, we investigated a regional ground subsidence in a parts of the Himalayan groundwater storage (HGS) system [19]. The HGS is a massive terrestrial water aquifer system in the Himalayan River basin [Fig. 1(a)]. Nearly one-fifth of the accessible freshwater is stored in the Himalayan region covering Indus and Ganges plains (IGPs) [20]. Due to orographic effects, seasonally variable monsoon climate has created a large water aquifer, especially around the Northern Punjab and Haryana provinces during the Holocene epoch [21]. However, excessive irrigation to feed the huge demands of the Northern Indian plains' agricultural

Manuscript received 19 December 2022; revised 15 June 2023; accepted 1 August 2023. Date of publication 15 August 2023; date of current version 8 September 2023. This work was supported by the National Science and Technology Council, Taiwan, under Grant NSTC 112-2625-M-004-001 and Grant NSTC 112-2420-H-004-007. The work of Tejpal Singh was supported by the Department of Science and Technology (Government of India) under Grant DST/INT/U.K./P-159/2016. *(Corresponding author: Shih-Yuan Lin.)*

Jungrack Kim is with Future Vision Inc., Icheon, Gyeonggi 12601, Republic of Korea (e-mail: kjrr001@gmail.com).

Shih-Yuan Lin is with the Department of Land Economics, National Chengchi University, Wenshan, Taipei City 116, Taiwan (e-mail: syl@nccu.edu.tw).

Tejpal Singh is with the CSIR-Central Scientific Instruments Organisation, Chandigarh 160030, India (e-mail: tejpal@csio.res.in; geotejpal@yahoo.co.in).

Ramesh P. Singh is with the School of Life and Environmental Sciences, Schmid College of Science and Technology, Chapman University, Orange, CA 92866 USA (e-mail: rsingh@chapman.edu).

This article has supplementary downloadable material available at https://doi.org/10.1109/TGRS.2023.3305863, provided by the authors.

Digital Object Identifier 10.1109/TGRS.2023.3305863

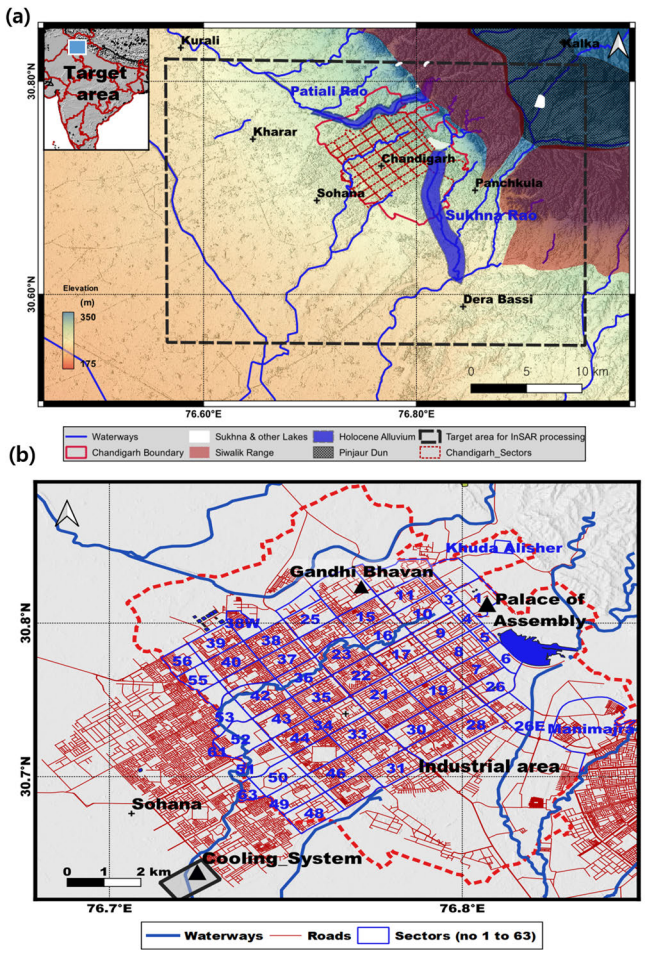

Fig. 1. (a) Location of target area and surroundings geographical/geological environments. (b) Sectors in Chandigarh city, roadways, and major interesting places.

complex caused the overexploitation of the HGS. Recently, Gravity Recovery and Climate Experiment (GRACE) data have been used in the northwestern parts of India, which have revealed depletion of groundwater storage (GWS) [2], [22] as well as involved ground deformation [23], [24]. Due to the limited spatial resolution of GRACE, the detailed distributions of groundwater depletion and consequent ground subsidence have not been well understood but are within the resolving scope of recent InSAR surveys [25], [26]. In recent years, the groundwater in the northern Indian cities, New Delhi [27] and Jagadhri [28], has been affected by subsidence, which was mapped by the InSAR time series analysis.

Our InSAR observation in the northwestern parts of India has shown a highly intensive ground subsidence around the Chandigarh city, which is not well investigated by any in situ or space geodetic methods. Together with the special location of Chandigarh in the cultural and economical context, it is important to investigate the spatiotemporal characteristics of ground subsidence in the region. We have conducted the InSAR campaign with two main objectives: 1) to study the geological/climatic contexts in comparison to long-term InSAR time series analysis to confirm the association with groundwater depletion and 2) the employment of two different time series InSAR techniques, i.e., persistent scatterer interferometry (PSI) [29] and New-Small BAseline Subsets (NSBASs) [30] to evaluate the potential hazard on the constructions assigned as historical heritages in Chandigarh.

II. Test Site

Chandigarh is a planned city constructed in the foothills of the Siwalik Range of the western Himalayas between Punjab and Haryana states [Fig. 1(a)]. Based on the innovative city planning concept introduced by Le Corbusier who built a major agenda of modern architecture and city planning, the city is built over a concrete base, intersected roadways in highly regular patterns, and ferroconcrete buildings [Fig. 1(b)]. Such city structures formed peculiar SAR scattering patterns and were applied in this study. Many architectures have been treated as monuments of modern building design. Among them, the Palace of Assembly was assigned as a UNESCO world heritage. Considering the ground subsidence associated with the water depletion, the safety of monumental buildings attracted our attention and became the main motivation of this study using InSAR analysis. The industrial sectors are located in the southern part of the central city area and several factories (paper, metal, and machinery) are in the area. The groundwater is used by the existing facilities and one million population. Furthermore, water is also used from Sukhna lake, an artificial lake damming a seasonal river, so-called Sukhna Choe that originates from the Siwalik Range. Over-water consumption and frequent depletion of seasonal inflow led to the shrinking of both Sukhna lake and possibly connected groundwater aquifer as well. The city is located in the southern piedmont of Siwalik Range, part of the sub-Himalaya, which is folded into an anticline topography overriding the Main Frontal Thrust (MFT) in the north of Chandigarh [31] that resides as the source of the fluvial water flow and sediments in the IGP. The young Holocene alluvium soils around two major "Rao (seasonal inflow channel)", i.e., Sukhna and Patiali Raos within Chandigarh city area [Fig. 1(a)] [32]. The alluvial aquifer system around the Chandigarh city area is highly complex, composed of alternating coarse and fine sands, silts, and occasionally clays, deposited within a sequence of channel and interchannel deposits. The complexity of the alluvial aquifer system is largely driven by the proximal–distal changes in fluvial processes over a variety of scales and typologies [33]. In particular, the Pleistocene and Holocene alluvium seen in the Chandigarh city area show significant sedimentological differences over short distances [33] that are characterized by a significantly higher proportion of finer alluvium sediments due to low-energy fluvial systems and relatively large distances between active river channels which limit the proportion of sands and gravels, to silts and fines. The proportion of the finer alluvium sediments increases swiftly toward the distal part away from the Siwalik Range. Such a fluvial system around our study area demonstrates dependence on the local groundwater supplies and economical processes.

Chandigarh is a typical subtropical area, dominated by the 70%–80% precipitation during the monsoon season (late-June–mid-September). The average high temperature is around 38 °C during the summer season. Over the year, the average

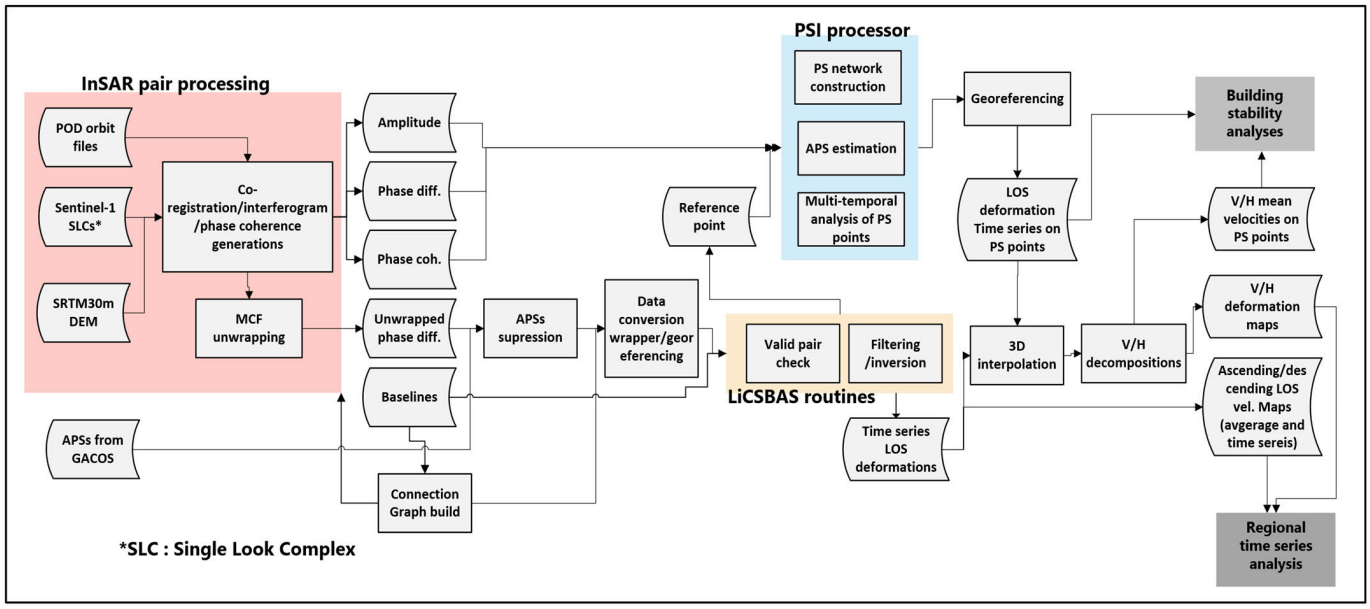

Fig. 2. Overall processing steps of InSAR time series analysis.

temperature is about 20 °C. This is important as we have made efforts to avoid InSAR data during the monsoon season due to the errors caused by the enhanced water vapor in the interferograms and thermal response of the structures.

III. Method and Datasets

In order to carry out a detailed analysis and to investigate the cause of ground deformation around Chandigarh, we followed the steps, as shown in Fig. 2. Furthermore, to understand the deformation based on a broader context, not only the center of Chandigarh city but also we have investigated the surrounding cultivated area in the process. Considering the capability to extract densified observations in vegetated areas as well as to achieve precise observation in the central city area, we used two different InSAR time series analyses. The results were integrated for further analysis.

A. PS and NSBAS InSAR Processing Method

The differential InSAR (D-InSAR) technique developed to trace surface change is based on the relation as follows:

$$\Phi_{\text{obs}} = \Phi_{\text{int}} + \Phi_{\text{topo}} + \Phi_{\text{E}} \tag{1}$$

where Φ_{obs} is the observed phase angle difference by InSAR pair, Φ_{int} is the phase angle difference by surface deformation, Φ_{topo} is the phase angle contribution by base topography which can be simulated and subtracted by base digital elevation model (DEM), and Φ_{E} is the phase error by various error factors. Therefore, Φ_{int} is convertible to the surface deformation once after Φ_{topo}, and Φ_{E} is corrected on the condition that other systematic noise is negligible.

The major challenge is to achieve precise InSAR analysis after evaluating error analysis. Error components are associated with the observed phase angle difference using the following equation:

$$\Phi_{\text{E}} = \Phi_{\text{a}} + \Phi_{\text{t}} + \Phi_{\text{o}} + \Phi_{\text{n}} \tag{2}$$

where Φ_{a} is the error term of the change of atmospheric condition, Φ_{t} is the base DEM error even after compensating Φ_{topo}, Φ_{o} is the orbital error, and Φ_{n} is the phase noise of systematic component.

To address error components, InSAR processing used time series analysis by stacking multiple interferograms. There are mainly two different time series approaches. One is to trace the temporal behaviors of strong reflectors, i.e., PS points by time series pairs formed by a single reference to multi-comparison image geometry, known as PSI [29]. In PSI, Φ_{E} is iteratively estimated into atmospheric phase screen (APS) over the PS point network. In contrast, SBAS [34] techniques form a series of intensive phase angle difference maps on small scattering objects, known as distributed scatterers (DSs), using multireference-to-multicomparison geometry. It should be noted that the concept of DS is valid even if a single reference geometry is applied in the stacking process. It corresponds to a linear system consisting of a small baseline combination matrix, phase values, and mean phase velocities. Singular value decomposition (SVD) together with low-pass (LP) and high-pass (HP) filters are used on a linear system to obviate the spatial and temporal components of the noise and to extract the error-reduced deformation. The resultant deformation velocity estimated from such linear operation has reduced the atmospheric, orbital, and base DEM noise, which are compensated by LP and HP filtering [35].

The density of DS processed by ordinary SBAS is not sufficient to monitor continuous deformation since the surrounding area is covered by the paddy field. The paddy field and natural vegetation together with other decorrelation factors, such as reconstructions and changes in topography, misregistration and day-to-day weather variability, lead to occasional breaks in connection of correlation covering all observations. Therefore, the inverted deformation by SBAS was limited to provide highly densified observations in time series analysis to trace regional deformation, which may be induced by ground subsidence. We have used NSBAS, an improved version of

SBAS technique, to avoid associated errors. NSBAS [30], [36] algorithm is used for the densification of reliable scatterers as shown from the intercomparison with other time series algorithms as discussed by Gong et al. [37]. Together with its capability of manipulating partially connected scatterers and producing superior observation point density, the NSBAS time series technique was applied.

Since the target area is covered by highly variable phase delay originated from atmospheric water vapor from orographic and monsoon precipitation, the atmospheric error in phase difference needs to be prescreened. Although it was usually solved by PSI and SBAS algorithms, the introduction of external APS datasets was implemented to remove the errors [38]. European Centre for Medium-range Weather Forecasts (ECMWF) Reanalysis-Interim [39] was used by Jolivet et al. [40] as the source of APS; they identified that the effects of such APS model employing ECMWF ERA is efficient to enhance time series analysis. Error compensations of each interferogram product were performed by subtracting APSs [41], [42]. In this study, we developed APSs using Generic Atmospheric Correction Online Service (GACOS) (http://ceg-research.ncl.ac.uk/v2/gacos/), which is developed on the ECMWF ERA-Interim model [43]. The APS was applied to each interferogram produced by the ESA Sentinel-1 toolbox (https://sentinel.esa.int/web/sentinel/toolboxes/sentinel-1) and minimum cost flow (MCF) unwrapping algorithms [22] combined with in-house batch processing wrapper. The processed interferograms and phase coherence were delivered to the NSBAS routine, so-called Looking into Continents SBAS (LiCSBAS) [44], by our own in-house data conversion wrapper. It should be noted that we used our own interferogram products instead of the products provided in Looking into Continents from Space with Synthetic Aperture Radar (LiCSAR) [43] service (https://comet.nerc.ac.uk/COMET-LiCS-portal/), which is originally distributed for the default use of LiCSBAS. There are two reasons to replace LiCSAR products with our own interferograms: 1) in comparison to LiCSAR products with 100-m spatial resolution, our own interferograms achieved 30-m spatial resolution; thus, the regional deformations could be traced with a better quality and 2) we were able to extend temporal coverage beyond that of the LiCSAR products, which covered only 2016–2017. The orbital error compensation is also necessary as described by Biggs et al. [45] and Wang and Jonsson [46]. Assuming a polynomial type of orbital error, the orbital inaccuracy caused the erroneous phase contributions to interferograms errors, and its consequent distortions can be approximated as follows:

$$f(R, A) = \sum_{i=0}^{2} \sum_{j=0}^{2} a_{ij} R^i A^j \tag{3}$$

where R and A are the range and azimuth, respectively, a_{ij} is the coefficient set which can be found through the least squared solution, and f is the error residual in the range (R) and Azimuth (A) domains. By adding this correction component, it is possible to remove the orbital inaccuracy of the phase angle. We checked first and second polynomial orbital errors and applied first-order correction considering the relatively narrow processing domain of our interferograms generated using the internal filtering stage of LiCSBAS. The influences of Sentinel-1 orbital errors on the InSAR processing are discussed by Yagüe-Martínez et al. [47] and Yague-Martinez et al. [48]. The use of DS-based analysis on the building stability of Chandigarh city area, especially for monumental buildings, is not adequate because the SBAS and NSBAS algorithms exploiting DS depend on only filtering for the eradication of Φ_t term, which can be induced by the height difference between base DEM and actual vertical building profiles, since part of them can be compensated by the angular diversity of perpendicular bases. Although there are some algorithms to combine PS and SBAS mainly to increase the density of observations [49], [50], we used simultaneous processing of PS and NSBAS in order to achieve both merits of PS and NSBAS for the observations of local/structural instabilities. A detailed investigation on the difference between SBAS and PSI is given in Sections IV and V.

The application of the PS algorithm begins with the discrimination of persistent scatterers (PSs) by measuring amplitude dispersion as follows:

$$\text{Disp(amp)} = 1 - \frac{M(\text{amp})}{\text{Std(amp)}} \tag{4}$$

where M(amp) is the mean deviation of amplitude, and Std(amp) is the standard deviation of amplitude in time series. The PS point network with Disp(amp) > 0.75 was constructed and iteratively estimated error components by nonlinear equations. In the adjusted model residual, each pair's APS was established and removed. After APS is eliminated, networks of PS points are extended until up to the final APS estimation. During this stage, two errors, i.e., DEM error between the base topography and the building roofs or facet together with the thermal expansion components are estimated simultaneously using the following relation [51]:

$$\Delta H = \alpha H_0 \Delta T \tag{5}$$

where H_0 is the height of object, ΔT is the temperature change, α is the coefficient of linear expansion, and ΔH is the change of building height caused by thermal expansion.

The construction of a reliable PS point network is a challenge in the case of nonlinear deformation as discussed in the earlier PS study [52], especially together with the consideration of thermal expansion. Therefore, we simply assumed linear deformation and introduced additional interpretations to analyze the differences between actual and modeled deformation.

To consider PS and DS simultaneously and conduct intercomparison, we used a certain relation between PSI and NSBAS. The straightforward approach was the delivery of reference points from NSBAS to PSI. The delivery of a reference point that was automatically created by LiCSBAS taking into account multiple scatterers' characteristics to the PSI process would guarantee the intercomparison of two different outputs with a controlled data range. Among multiple combinations of reference points in ascending and descending modes, which are created by LiCSBAS routines, we chose the reference points set that minimizes the deformations in the northern target area, in which no deformations were observed [25], [26].

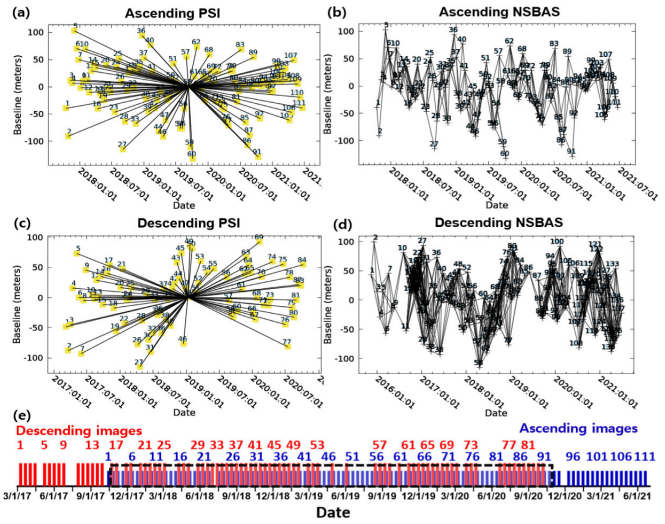

Fig. 3. Connection graphs of employed. (a) Sentinel-1 InSAR ascending for PSI. (b) Sentinel-1 InSAR ascending for NSBAS. (c) Sentinel-1 InSAR descending for PSI. (d) Sentinel-1 InSAR descending for NSBAS. In total, 111 ascending and 84 descending pairs were employed for time series analysis as shown in (e). Black dotted box represents the time domain used for decomposition.

The integrated InSAR was assessed and interpreted in comparison to geological/climatic/hydraulic information following the processing steps as shown in Fig. 2.

The groundwater withdrawal causes subsidence, in both the horizontal (H) and vertical (V) directions. However, vertical deformation is dominant for the most of subsidence due to compressibility, if the target area is not related to faults or fractures [15]. Upon line-of-sight (LOS) geometry of the SAR sensor, it is feasible to decompose horizontal/vertical deformation from the combination of ascending and descending InSAR outputs. The contribution of north–south directional deformation is considered minor as the orbits of Sentinel-1 is almost parallel to the north–south direction [53].

The V/H decomposition is obtained by following the relationship given by Fialko et al. [54]:

$$\begin{vmatrix} \mathrm{LOS}_{\mathrm{asc}} \\ \mathrm{LOS}_{\mathrm{des}} \end{vmatrix} = \begin{pmatrix} -\sin\theta_{\mathrm{asc}}\cos\alpha_{\mathrm{asc}} & \cos\theta_{\mathrm{asc}} \\ -\sin\theta_{\mathrm{des}}\cos\alpha_{\mathrm{des}} & \cos\theta_{\mathrm{des}} \end{pmatrix} \begin{vmatrix} D_H \\ D_V \end{vmatrix} \quad (6)$$

where $\mathrm{LOS}_{\mathrm{asc}}$ and $\mathrm{LOS}_{\mathrm{des}}$ are the measured LOS surface deformations in ascending/descending mode InSAR processing, respectively, D_H and D_V are the horizontal and vertical deformations, θ_{asc} and θ_{des} represent the incidence angles, α_{asc} and α_{des} are the heading angles, asc and des represent the ascending and descending geometries, respectively,. It should be noted that incidence angles have differences for whole image domains; thus, we used gridded incidence angles for the decomposition.

We only considered the ascending/descending LOS components within an overlapped time span, as shown in Fig. 3(e), for decomposition. We have applied a least squares quadratic fit with a second-order polynomial form to synchronize ascending/descending observation in common timings together with a offset to adjust little temporal mismatch between selected ascending/descending time coverage as developed by Yun et al. [55]. The referenced time frame is descending mode; thus, ascending mode datasets were interpolated.

TABLE I
SPECIFICATIONS OF EMPLOYED SENTINEL-1 IMAGES

Mode	Ascending	Descending
Image number	111	84
Reference Image	2019/07/01	2019/01/10
Time coverage	2017/10/15-2021/06/20	2017/03/09-2020/10/07
Heading angle (Northward)	-12.71 deg.	-167.32 deg.
Incident angle	39.29 deg.	39.30 deg.
Path/Frame	27/96	136/491
Acquisition time	12:55 UT (18:25 IST*)	00:51 UT (06:21 IST)
Polarization	VV** + VH	VV** + VH

* IST: Indian stand time; ** only VV mode was used for InSAR processing

B. Datasets Description

Owing to the availability in required spatiotemporal domain and open data accessibility, the Sentinel-1 SAR constellation was chosen as the InSAR data source. The wide coverage (Swath >250 km) and considerably good spatial resolution (20 m in azimuth and 4 m in range) acquired by Interferometric Wide-swath mode (IW) operation [56] are found to be the advantages of the Sentinel-1 images. A high temporal resolution of 12-days revisiting time enables to use a total of 112 and 85 images (Fig. 3 and Table I), respectively, acquired in ascending and descending modes for 3–4 years. The connections and temporal coverages were shown in Fig. 3. The orbit ephemerides files by Precise Orbit Determination (POD) service for Sentinel-1 (https://s1qc.asf.alaska.edu/aux_poeorb/) were applied to all Sentinel-1 images for better quality registration. Our target area was covered by only the second subswaths (IW2) of the corresponding Sentinel-1 frame and relative orbits for both ascending and descending modes, so it was straightforward to process these images. For the construction of base topography, we considered both 1-arcs Shuttle Radar Topography Mission (SRTM) and Copernicus DEMs (https://spacedata.copernicus.eu/explore-more/news-archive/-/asset_publisher/Ye8egYeRPLEs/blog/id/434960). The test shows no considerable height difference (>1 m) areas between the two DEMs. As we have no information regarding Copernicus DEM accuracy, the 1-arcs SRTM DEM was employed for InSAR processing. For the validation of PSI data, we used a Landsat-8 multispectral image of October 2020. All available groundwater level (GWL) is taken from the Central Ground Water Board (CGWB) (http://cgwb.gov.in/GW-Year-Book-State.html) and the water resource information system (https://indiawris.gov.in/wris/) to interpret InSAR in terms of piezometric contexts. A 0.25° resolution precipitation data (https://www.imdpune.gov.in/Clim_Pred_LRF_New/Grided_Data_Download.html) which is available from the Indian Meteorological Department for four years, i.e., 2017–2020 was used as complementary of groundwater datasets [57].

IV. Processing Results and Analysis

A. PS and NSBAS Results

NSBAS processing produced highly similar LOS deformation maps in both ascending and descending modes [Fig. 4(a) and (c)], indicating that the deformations were mostly induced by vertical subsidence. The average phase coherence maps shown in Fig. 4(b) and (d) provide information about the densified scatterer distribution over the Chandigarh city area as well as background paddy fields due to regularly populated villages and buildings, which are optimal as landmarks for NSBAS inversions.

PS processing with the delivered reference points from NSBAS routines was shown in Fig. 5(a) and (b). We also observed similar deformation patterns in both ascending and descending modes. PS and NSBAS were highly correlated and the details of intercomparison between PS and NSBAS were further discussed in the following section. Phase coherences and standard deviation of velocities presented in Supplement S.1 show a portion of unstable scatterers populated outside of Chandigarh city. Overall InSAR time series processing qualities were reliable as implied in maps of phase coherence and standard deviation of velocity.

B. Regional Classifications

As discussed in Section III-A, we further conducted vertical/horizontal decomposition using (6). The vertical deformation is found to be the dominant component (Fig. 6) compared with the horizontal deformation, which shows weaker migration compared with the vertical deformation (Supplement S.2). Therefore, we concentrated on vertical deformation, and this is identified as subsidence hotspots around Sohana, Kharar, and Dera Bassi (Fig. 6).

The deformation within Chandigarh city boundary is analyzed through the ten regions of interest (RoIs), as shown in Fig. 6; here, underground water pumping was the main water supply for the use. As no GIS data correctly assigns seasonally activated rivers and creeks that might indicate Paleocene/Holocene hydrologic activities and their sedimentary deposits, we also defined the hydrological channels based on topography, optical image, and local information (Fig. 6).

The RoIs consist of three groups on the interpretation of deformations that are shown in Fig. 7(a)–(c) as follows.

1) *RoIs(h):* The cores of major vertical deformation, defined as "hot spots," and acronym defined as h, over Sohana, Kharar, and Dera Bassi.
2) *RoIs(w):* In-between hot spots, a few relatively weak subsidence places named as Sohana (weak—short form defined as w), Kharar(w) and Dera Bassi(w).
3) *RoIs(ch):* Fours RoIs within Chandigarh city areas as named Ch. areas 1–4.

Their temporal behaviors in terms of GWL and consequences in the structural instability are further analyzed.

V. Discussion

A. Interpretation to the Climatic/Hydrological Factors

The ground water level is being monitored by the CGWB over the whole India. In the study area, data are sporadically available in the spatiotemporal domain. Therefore, we introduced GWS derived from the GRACE satellite to validate the InSAR observation. The change in GRACE GWS is derived from

$$\Delta\mathrm{GWS} = \Delta\mathrm{TWS} - (\Delta\mathrm{SM} + \Delta\mathrm{SR}) \tag{7}$$

where TWS is the change of total water storage in GRACE, SM is the soil moisture, and SR is surface runoff extracted from Global Land Data Assimilation System (GLDAS) Noah model [58]. See Supplement S.3 for the detailed procedure in GRACE GWS. The analysis of GRACE data has shown a pronounced declining of groundwater in the northwestern parts of India [21], [22], [60]. Although there are numerous studies using GARCE GWS and the InSAR signals comparatively on the water depletion area [22], [59], we considered the poor resolution of GRACE data (resolution 50 000–200 000 km^2) [60] and InSAR observation area (1000 km^2) in the present target area. Therefore, GRACE GWS around Chandigarh is first compared with the average GWL data obtained from CGWB and rainfall data over the Chandigarh city area.

Instead of the unavailable time series GWL, as the CGWB data are sporadic to be directly compared with InSAR data (see Supplement S.4), we mainly used monthly rainfall data in 0.25° resolution as a comparison time series.

Fig. 8(a) shows a declining trend of water storage from 2009, a pronounced decline was observed since 2016. The trend of GRACE GWS of 20 years is correlated with rainfall and GWL. It is known that the decline of rainfall after 2016 leads the unrecovered damage in groundwater aquifers [Fig. 8(a)]. The correlation between GRACE GWS and underground water level is 0.507 while GRACE GWS and rainfall during monsoon season is 0.638 with roughly half year time lag. Therefore, it indicates that GRACE GWS can be feasible as a GWL designator. The comparison with the InSAR LOS deformations in the whole area and the main subsidence area in RoIs(h), in Fig. 8(b) and (c) respectively, showing the validity of InSAR and the clues of the involved mechanism. In the full test area, InSAR LOS deformations followed the GRACE GWS (correlation value is 0.655 in ascending mode and 0.705 in descending mode) and show a partial relaxation in ground subsidence rate after the monsoon season. Thus, it fits our observation in Fig. 7. However, we also identify the InSAR LOS deformations in the main subsidence areas, i.e., RoIs(h), that have been continuously accumulated following the linear trend of GRACE GWS [Fig. 8(c)] and maintains even higher correlations (correlation value is 0.764 in ascending mode and 0.811 in descending mode). It implies that a strong driver of different subsidence patterns has different regional subsurface sedimentary architecture as explained beforehand. The involvement of in situ GWL with InSAR deformations is not clear as shown in Supplement S.4 which employed different quantities, such as LOS velocity and GWL fluctuations. It is mainly because the measurements of GWL were often contaminated with artificial water recharged while the observations itself is very sporadic. We applied the analyses using spatial analyses based on the GWL trend data which is available in the Indian water resource information system (IWRIS), as shown in Supplement S.5. However, the miss-match between InSAR

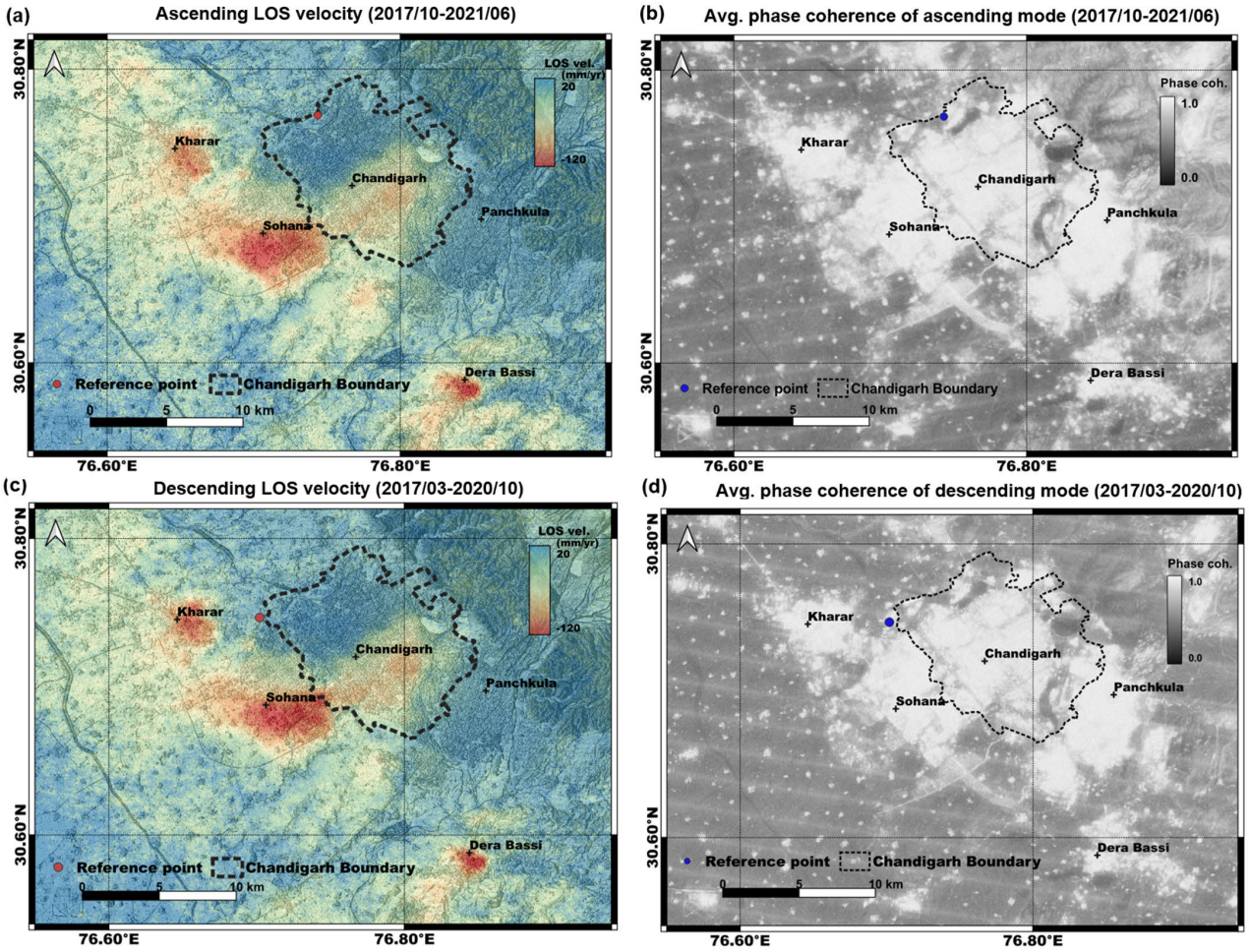

Fig. 4. (a) LOS deformation by NSBAS descending mode. (b) Phase coherence map of NSBAS descending mode. (c) LOS deformation by NSBAS ascending mode. (d) Phase coherence map of NSBAS ascending mode. Note that the reference points in ascending and descending modes were delivered to PS processing.

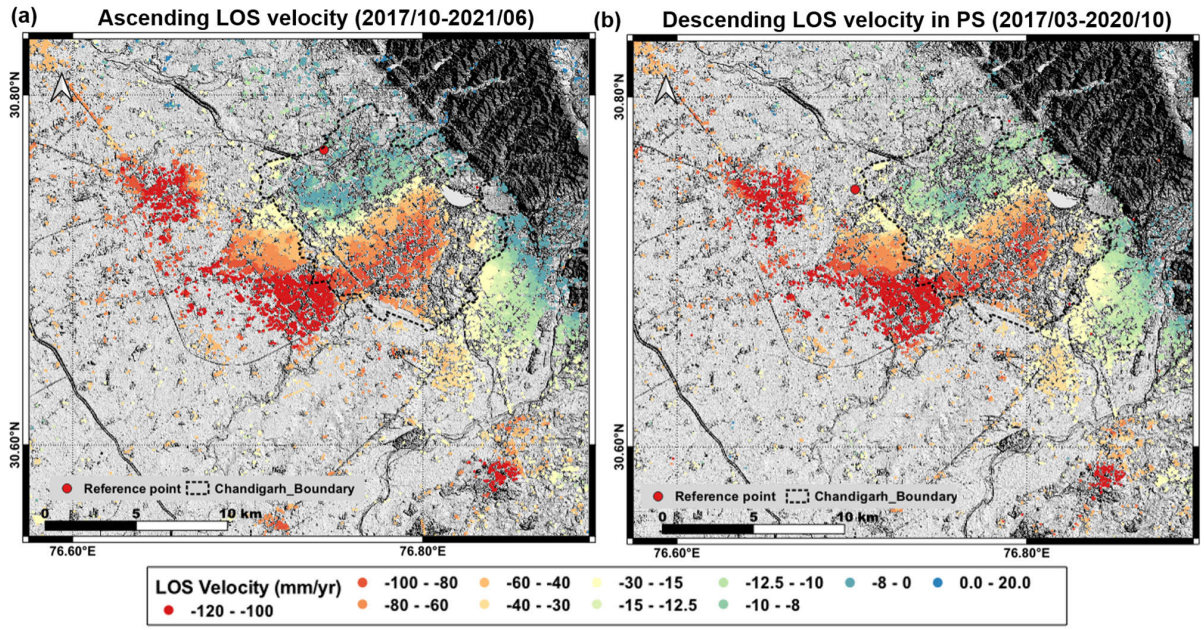

Fig. 5. LOS deformation estimated by PSI. (a) Ascending mode. (b) Descending mode. See Supplement S.1 for maps of phase coherence and standard deviation of PS velocities.

deformation and GWL trend around Sohana needs to be interpreted more. Also, we were not able to precisely interpret temporal behaviors of InSAR LOS involving GWL due to the deficiency and contamination of observation. Therefore, we further applied the modeling of periodicity and geological analyses.

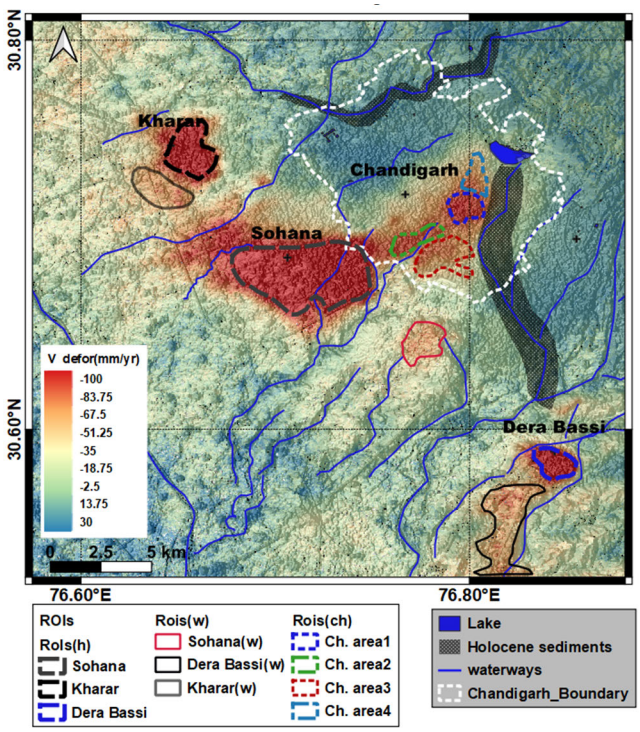

Fig. 6. Mean vertical deformation velocity estimated by NSBAS decomposition (2017/10–2020/10).

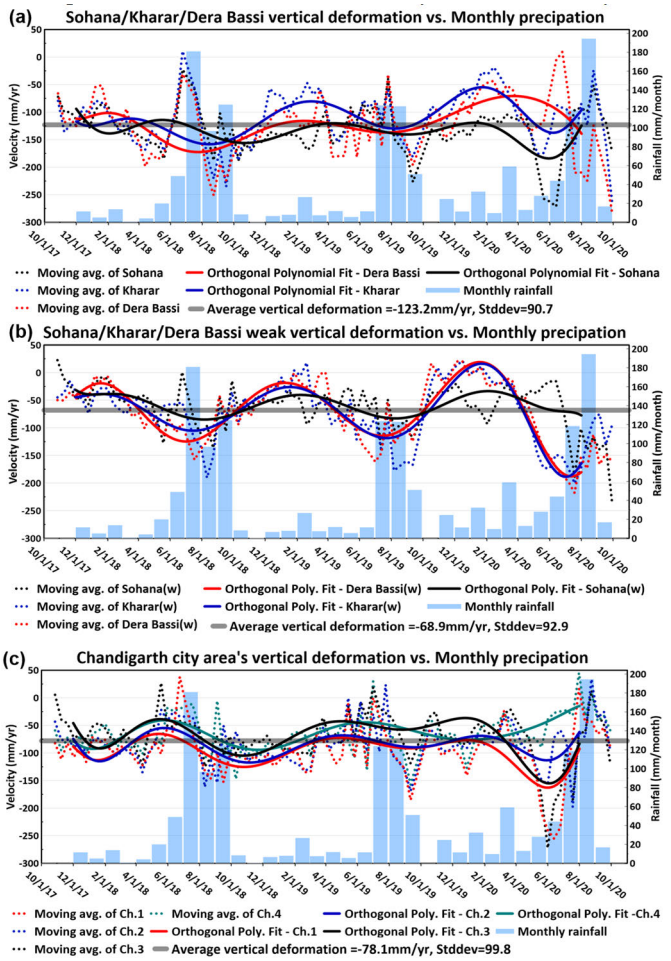

Fig. 7. (a) Vertical deformation profiles over three subsidence hot spots, i.e., RoIs(h). (b) Vertical deformation profiles over three weak RoIs, i.e., RoIs(w). (c) Vertical deformation profiles over four Chandigarh RoIs, i.e., RoIs(ch). Since the deviations of observations are high, we used window moving average and a sixth-order orthogonal polynomial fit for the further analyses.

B. Periodicity Model

The group of RoIs possessed different periodicities. For instance, RoIs(w) is represented in orthogonal polynomial fitting [Fig. 7(b)] for a one-year period with the maximum subsidence during June–August and minimum subsidence during February–April. We analyzed temporal responses of RoIs with the involvement of hydraulic contexts. Compared with monthly local rainfall data of 0.25° resolution, we found that the introduction of a six-month time lag in order to respond to the heavy rainfall into the relaxation of subsidence was able to justify the observed periodicity and the time lag in RoIs(w). The periodicities in RoIs(h) or RoIs(ch) are not very clear. However, as shown in Fig. 7(a) and (c) for RoIs(h) and RoIs(ch), respectively, the prompt but partial restoration of subsidence in the monsoon season was observed. Here, we proposed a model: 1) RoIs(ch) consisting of weak yearly periodicity of poor and strong monsoon seasonal prompt subsidence, which were referred to as yearly lag subsidence (YLS) and pulse response subsidence (PRS); 2) RoIs(w) is mainly dominated by YLS component; and 3) RoIs(h) is under combined influences by both YSL and PRS.

The model is further validated by the introduction of periodicity decompositions as shown in Fig. 9. The methodology of periodicity decompositions was based on seasonal and trend decomposition (STL) using locally estimated scatterplot smoothing (LOESS) [61]. We used a simple additive model as given in the following equation:

$$D[t] = D_T[t] + D_S[t] + D_E[t] \tag{8}$$

where $D[t]$ is the time series of deformation, $D_T[t]$ is the trend of the deformation time series, $D_S[t]$ is the seasonal component of the deformation time series, and $D_E[t]$ is the error residual of the STL model. LOESS was initially used for the smoothing of datasets and iteratively optimized the trends and the seasonal components.

Once we applied STL over vertical migrations of RoIs, the clear periodicities were revealed, which fit our assumed models. We employed linear models in trend data and orthogonal polynomial regressions in seasonal data to understand patterns. In Sohana, RoIs(h) showS strong vertical deformation up to 130–150 mm/year for two years, strongly contrast to the relaxation trends in Kharar and Dera Bassi [Fig. 9(a)]. Perhaps the groundwater pumping from the shallow aquifer (static water level is close to 9.7 m according to the IWRIS) for cooling systems in Sohana is the main cause for enhancing vertical deformation. The seasonal periodicity represented as the form of sinusoidal wave with one-year period and half-year time lag to the monsoon, the YLS is clearly observed in the case of RoIs(w) [Fig. 9(b)] with 50–100-mm/year magnitudes, which is also observed in the second regressions of RoIs(h) and RoIs(ch) with 40–80-mm/year magnitudes although those are overlapped with PRS. PRS can be identified by the seasonal decomposition in both RoIs(ch) and RoIs(h) with 100 mm during the 4–5 months' monsoon period in comparison to their second-order regressions presenting YLS.

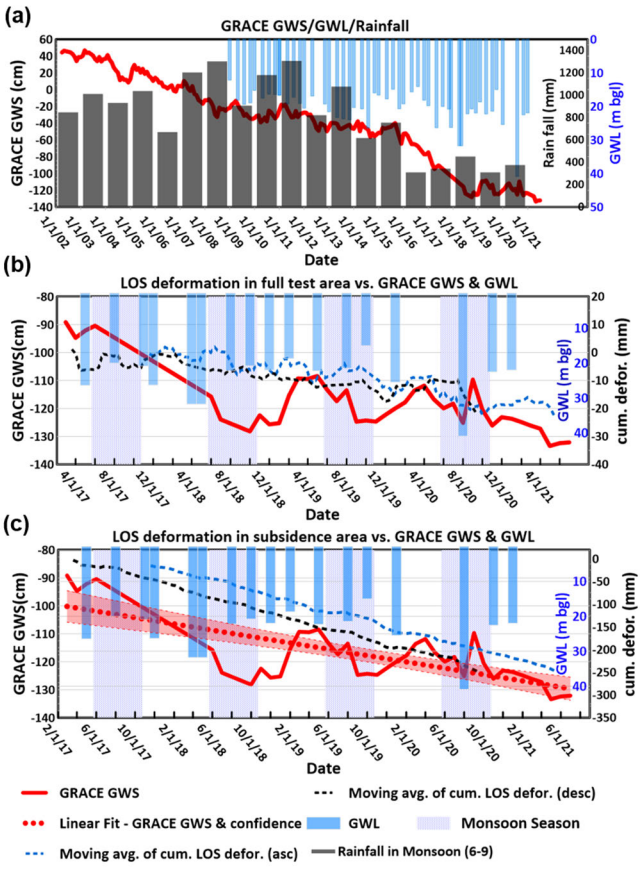

Fig. 8. (a) GRACE GWS/GWL/Rainfall time series for 20 years. There was no time lag between the signals. (b) Cumulative deformation/GRACE GWS/GWL time series over the whole test area. A time lag in six-month was found between the upward deformation of LOS and GRACE GWS. (c) Cumulative deformation/GRACE GWS/GWL time series on major ground subsidence area (see Fig. 9). LOS deformations follow GRACE GWS and are continuously accumulated. Here, the GWL unit is a meter-to-ground level (m · bgl).

The interpretations of such periodic behaviors of deformations were discussed in the following.

C. Geological Interpretation

The characteristic behaviors of ground subsidence (Fig. 6) in different RoIs are discussed for three different geological and hydrological environments.

The alluvial stratigraphy shows a high degree of spatial variability of the Indo–Gangetic plains from west to east, and the thickness of the alluvial sediments and bedrocks also vary at the local scale [33]. This corresponds to the strong spatial heterogeneity of groundwater depletion, discharge of river sediments, and geomorphology [62]. In particular, the test sites around Chandigarh city center are characterized by high variability in GWL due to the limited and highly heterogeneous distribution of aquifer sediment in the subsurface and with the population density consuming more water [54], [55]. In Chandigarh, groundwater is being tapped from deep aquifers that are confined to nature. This is in contrast to the surrounding regions of Kharar, Sohana, and Dera Bassi tapped from shallow and deep aquifers. Here, the groundwater occurs under phreatic conditions in shallow aquifers, whereas leaky confined-to-confined conditions exist in the deeper aquifers [63]. In spite of strongest vertical deformation associated with heavy and delayed compaction of aquitard, it is difficult to track the GWL trend (as shown in Fig. 9) around Sohana due to artificial recharges, geological, and hydrological variability.

The northern RoIs(ch) with a quick, strong but short aquifer response suggests the role of the proximal piedmont with high hydraulic conductivity (cobble, pebble, and boulder, associated with sand, silt, and clay). This should facilitate swift percolation of water which readily recharges the shallow aquifer in the proximal part (piedmont of the Siwalik range) corresponding to the northern RoIs(ch). Further south corresponding to RoIs(w) region, the weak response suggests a significant reduction of hydraulic conductivity by several orders (Fig. 9). This would indicate a systematic and gradual thinning of the shallow aquifer further away from the recharge zone of the Siwalik range. As suggested above, the thinning of the shallow aquifer zone which is a proxy to the paleotopography where the percentage of coarse components reduces away from the Siwalik range [64]. This explains the PRS in the RoIs(ch) and the absence of PRS further south corresponding to the RoIs(w). Thus, the PRS signal in RoIs(h) is indicative of a highly variable aquifer geometry, locally producing a strong response.

The YLS signal does not directly relate to the recharge by monsoon; instead, the response is delayed by around six months (Fig. 9). A similar pattern is observed in all three RoIs that suggests that the involved aquifers are replenished over a period of six months following the monsoon (i.e., only during the winter seasons). This shows lag response over a large area indicating a linkage with a large and deeper aquifer system. In the RoIs(ch) region, the deep aquifers are confined in nature, whereas, in the RoIs(w) and RoIs(h) region, the deep aquifer is leaky confined to confined in nature [63]. The groundwater drawdown in the RoIs(ch) is mainly limited to human consumption and limited industrial use. This is significantly lower compared with RoIs(h) and RoIs(w) (Kharar and Dera Bassi blocks) which are overexploited blocks. It is notable that the groundwater draft for agriculture has decreased over time but the draft for industrial and domestic usage has increased tremendously [63]. This is also in-line with the rapid urbanization trend in the whole of Punjab state, where built-up area has increased by 372.27 ha (112.04%) [65]. The difference in groundwater drawdown matches well to a weak YLS corresponding to RoIs(ch), whereas a strong YLS corresponds to RoIs(h) and RoIs(w). However, the variability in the InSAR signal from RoIs(h) and RoIs(w) is similar to the response of pumping from the distal part of a narrow set of aquifer bodies that may lead to greater depletion in adjacent areas that lack such abundant and thick aquifer bodies [66]. An uplift area up to 25 mm/year in Chandigarh and another in Panchkula (Fig. 6) was observed due to recharges by incised channels from Siwalik range, which was also presented in GWL trends of Fig. 9. The elastic rebound as a major mechanism of such uplift is discussed by Chen et al. [67] and Neely et al. [68].

D. Building Stability Analysis Using PS

The building stability check in ground subsidence area has been a long-time topic of PSI technique [69], [70]. Despite

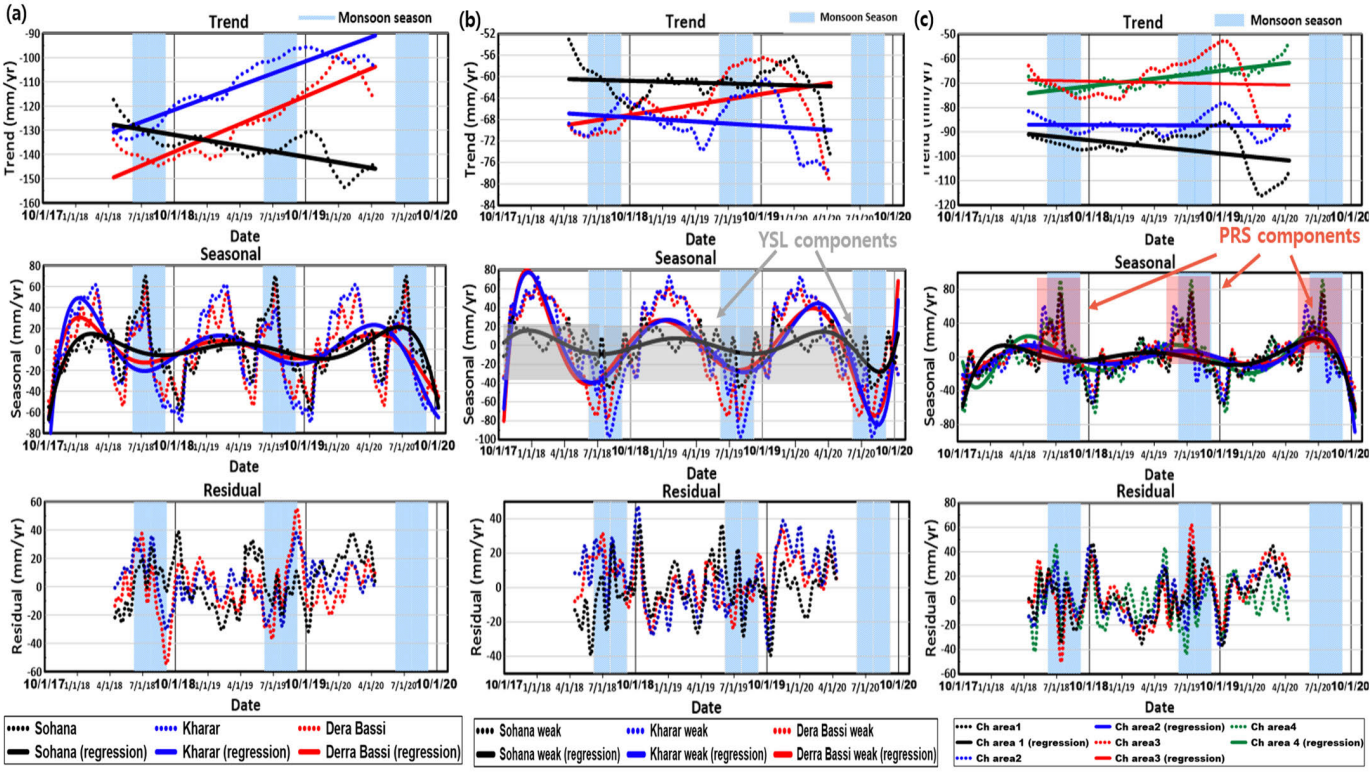

Fig. 9. Periodicity decomposition over RoIs. (a) Trend, seasonal, and residual points over RoIs(h) and their second regression models. (b) Trend, seasonal, and residual points over RoIs(w). (c) Trend, seasonal, and residual points over RoIs(ch). Note that we used a linear model in trend data and a sixth-order orthogonal polynomial regressions in seasonal data.

high-density PS observation, the tasks, in the case of Chandigarh, were problematic due to issues such as thermal expansion and an abnormal population of scatterers. The correlation analysis between PS and NSBAS is shown in Fig. 10. The LOS velocities estimated from PS and NSBAS were highly correlated by linear forms [shown in Fig. 10(a) and (b)]. The correlation in decomposed V velocities was identified, but H velocities of NSBAS and PS are not found to be correlated. To clarify the relationship between NSBAS and PS, we concentrated on the deviated scattering points which are detected by a criteria of standardized regression error (>1.0 in this case). Presumably, those PS points deviated from the clear linear relationship became the candidates of our further analysis, because the velocity deviation of PS points from NSBAS regional components was likely induced by the independent structural migration. The deviated PS and NSBAS points in both ascending and descending modes were projected in the spatial domain and identified in strong vertical deformation areas observed in NSBAS over Chandigarh to Sohana and Kharar belt [Fig. 10(e) and (f)].

In parallel to the PS–NSBAS correlation analysis, we introduced another quantitative approach based on PS point classification [71]. We considered the time series deformation trends of these PS points into account, as well as the spatial clustering of PS points, to classify all PS points into categories. To implement the classification, the data were aggregated and summarized into a space-time cube. The 3-D cube was made up of space-time components to the base constructed by the planimetric coordinates of the PS points covering Chandigarh, and the vertical dimension was formed by the acquisition dates of each Sentinel-1 image. The trends of displacement recorded in these spatial clusters were further evaluated using the Mann–Kendall trend test [72]. We have further classified the trends as "stable" as those fit the distributions of no-subsidence/no-deviated PS points and mainly considered negative directional classes as "unstable" (refer to Supplement S.6 for details of identified classes of PS points and their characteristics).

We overlaid the classified PS points over the built-up mask created by Landsat-8 built-up index (BI) combining the normalized BI (NDBI) and normalized vegetation index (NDVI) using the following relation [73]:

$$\mathrm{BI} = \mathrm{NDBI} - \mathrm{NDVI} = \frac{\mathrm{SWIR} - \mathrm{NIR}}{\mathrm{SWIR} + \mathrm{NIR}} - \frac{\mathrm{NIR} - \mathrm{Red}}{\mathrm{NIR} + \mathrm{Red}} \quad (9)$$

where SWIR is the short-wave infrared band (band 6 in Landsat 8), NIR is the near-infrared band (band 5), and Red is the red band (band 4). The threshold value of BI was 0.28 referencing the outlines of incomplete building footprint in OpenStreet map. By masking off nonbuilt-up areas using BI, the class types of PS points over Chandigarh were identified. It was found that southern Chandigarh mainly included the class types which were assigned as unstable PSs (refer to Supplement S.6 for the distribution of classified PS points).

We have focused our study on the migrations of PS observations. As the instability in base topography causes the weakness of the lower part of the building [74], [75], [76], the horizontal deformation (so-called "tilting") by decomposition of ascending/descending PS represents the instability of buildings. Our approach is to manage the decomposition of ascending/descending PS within independent structures.

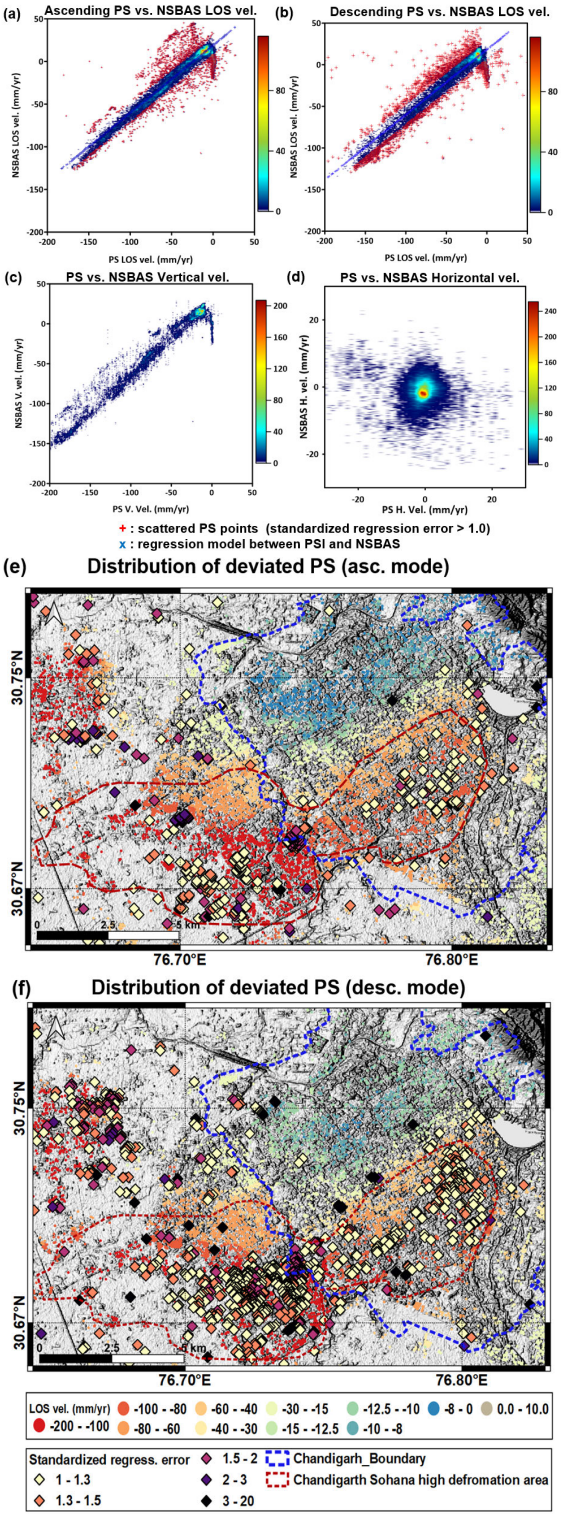

Fig. 10. (a) NSBAS versus PS velocity in ascending mode LOS observation (correlation value in two components is 0.958). (b) NSBAS versus PS velocity in descending mode LOS observation (correlation value: 0.939). (c) NSBAS versus PS velocity in vertical deformation (correlation value: 0.940). (d) NSBAS versus PS velocity in horizontal deformation (correlation value: 0.582). (e) Spatial distribution of the deviated PS points [refer to red crossed points in (a) and (b) whose standardized regression error >1.0] extracted from ascending mode observation. (f) Spatial distribution of the deviated PS points extracted from descending mode observation.

Then, we traced temporal behaviors of ascending mode LOS deformations of target structures since the temporal coverage of descending mode, as well as PS point density, was not adequate to assess recent deformation patterns. The algorithm to conduct structural PS decomposition is shown as follows.

1) Define labeled segments on the built-up mask mentioned above by masking-off road networks with a buffer zone (10–20 m according to the grade of roads).
2) Further mask-off on labeled segments with water, park, and railways.
3) Overlay some available building footprints on the segments and define further structural segments. Therefore, a total of 8024 structural segments were defined around the Chandigarh city area.
4) Allocate DEM error points which extracted by PS processors as follows [77]:

$$\Delta H = \frac{\lambda}{4\pi}\frac{r\sin\theta}{B}\Phi_{\text{topo}} \tag{10}$$

where is the wavelength, r is the slant range, and B is the perpendicular baseline.

5) Adjust the segment locations using the following relation [78]:

$$\Delta x = \Delta H \cot\theta \cos\alpha \text{ and } \Delta y = \Delta H \cot\theta \sin\alpha \tag{11}$$

where Δx and Δy are the EW and NS positional adjustments.

6) Allocate PS points in ascending and descending modes on the structural segments.
7) According to the number of PS points (N), perform gridding, i.e., inverse distance weighted (IDW) if $N > 3$; otherwise, median value fill.

We have considered most of the structural segments, which are filled with representing PS values in both ascending and descending modes. Applying (6) together with incidence angles on segments, we created vertical/horizontal (so-called H and V) velocity maps, as shown in Fig. 11. The interesting things in the analyses of Fig. 11 additionally in comparison to PS point classifications and PS-NSBAS correlation analysis are as follows: 1) the most significant H-valued areas such as sectors 18, 34, and 45, exist along the boundaries of high deformations area which are defined by NSBAS; 2) the deviation points of PS-NSBAS fit part of high H values areas which exists on high V migrations; and 3) PS point classification as sporadic subsidence of ascending mode fit the H migration of 1. There is no direct correlation between H and V velocities. We concluded that the structural instabilities presented in horizontal titling were often caused by sporadic subsidence on the boundary of uplift and subsidence. On the other hand, the central parts of vertical subsidence also cause instabilities in the strictures. The structural instabilities in Sohana and Kharar might be due to weak foundations of local housings overlapped with strong vertical subsidence. It is worth noting that the cooling system in Sohana induced strong structural instabilities. After all, the decomposition analyses of PS using structural segments demonstrated the concealed instabilities from NSBAS. It is because PS captures and monitors the scattering from a single object than the synthesized response by NSBAS as demonstrated by Yan et al. [79].

The cumulative deformations and velocity patterns of PS over the proposed structural instability areas, which correspond to the sectors 18, 30, and 34, together with interested

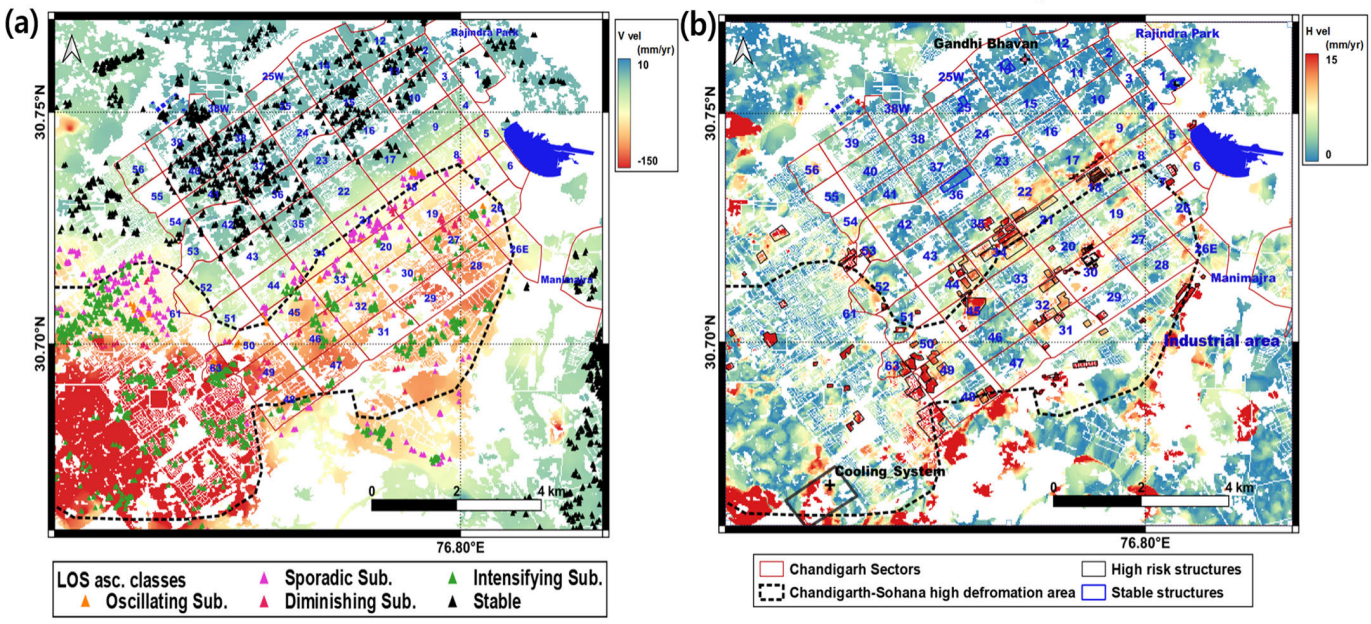

Fig. 11. (a) V migration of individual structures with classified PS points. (b) H migration of individual structures. Refer to Fig. 12 for the temporal behavior of the specific structures. Also, refer to Supplement S.7 for the details.

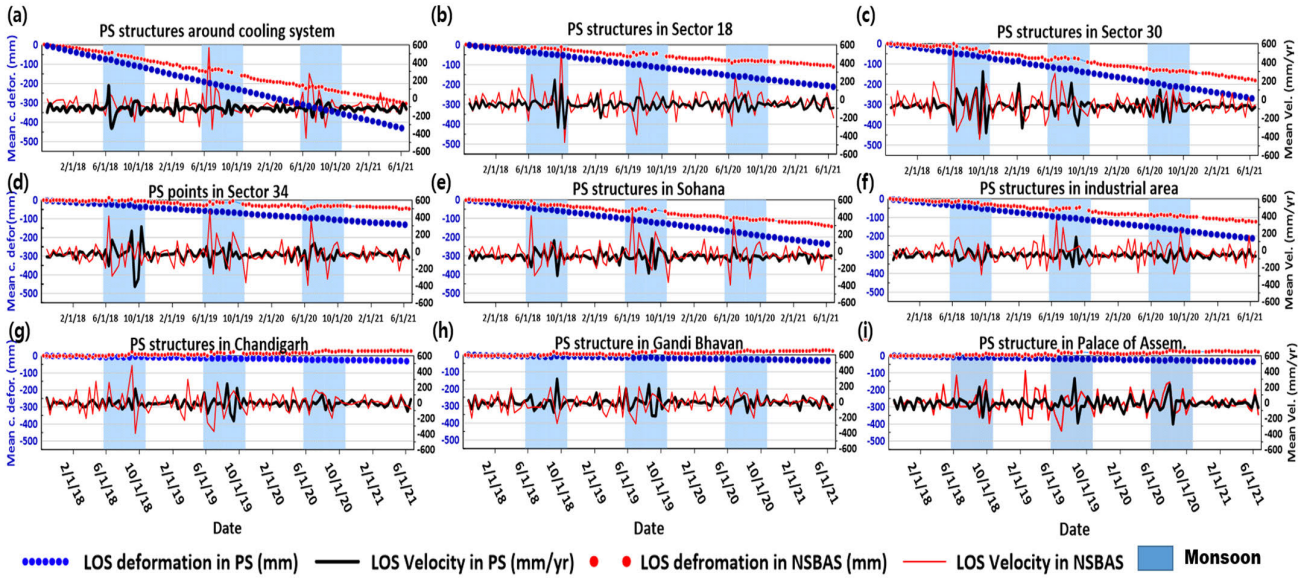

Fig. 12. (a) Patterns of cumulated deformations and velocities in ascending LOS over the structures of cooling system. (b)–(f) Other structures of strong H-trending structure (H velocity >10 mm/year). (g)–(i) Structures with stable trend (V and H velocities <5 mm/year) including Gandi Bhavan and Palace of Assembly. Note that the locations of structures can be seen from Fig. 11. The NSBAS profiles were taken from buffered (<150 m) zones of PS structures but excluded other structures.

places, such as cooling system, industrial sectors, monumental buildings (i.e., Gandhi Bhavan and Palace of Assembly) were shown in Fig. 12. After all, we identified H migration structure that presents the most variant velocity profiles in Fig. 12(a)–(f), might be related to the tilting of structures induced by highly variable deformations. As shown in Fig. 12, the variances of velocities are maximized up to 100–600 mm in the monsoon season (late June–early September). It implies that the stability of the structure is a consequence of nonlinear vertical migrations during monsoon seasons. The velocity of pattern of the cooling system in Fig. 12(a) is highly obvious, showing consistently strong subsidence as a consequence of the pumping from shallow water aquifer. We noted that it created extensive instabilities in the vicinity as well as the cooling system location. The structures in Shahana and industrial areas also possess consistent subsidence but not significant velocity variations, perhaps due to the less loading imposed by low relief structures [Fig. 12(e) and (f)].

We proposed that not all strong V directional migrations evolved into immediate hazardous areas as it takes considerable time that equally strong regional subsidence cause inherent structural risk of individual structures, which can be revealed as the forms of horizontal tilting. The mechanism inducing horizontal tilting is highlighted when we compare NSBAS deformation patterns to PS ones demonstrated in Fig. 12. The deformations in NSBAS observations often

rebounded with heavy precipitations during monsoon that can be explained by a few experiments and observations [27], [80], [81], but the rebounds in structures by PS are not strong, perhaps due to the loading of building structures. It explained that the low variability and higher deformations of PS are compared with NSBAS observations (Fig. 12). The unresolved structural stresses may develop into horizontal tilting. The deformation patterns in the Palace of Assembly as well as Gandhi Bhavan, neither show risky deformation patterns, as demonstrated in Fig. 12(h) and (i) nor horizontal tilting. However, our subsidence analysis shows a considerable deformation to LOS 50 mm in the very recent epoch in the monumental buildings of the Palace of Assembly [Fig. 12(i)]. Moreover, the velocity variations of the two places are not negligible due to the seasonal monsoon recoveries and regional elastic rebound [67]; thus may develop into structural instability. Therefore, we suggest continuous monitoring of structures, especially the valuable architectures in Chandigarh city that will help to take an appropriate measure to protect these valuable structures, which have an archeological value.

VI. Conclusion

Our study is based on detailed analysis of InSAR time series, and their spatiotemporal interpretation around the Chandigarh city area that show ground subsidence up to 120 mm/year. The intercomparison to geological, hydrological, and climatic information by the correlation analysis show pronounced subsidence induced by groundwater depletion, which is also supported by the GRACE data but is not well identified in detail with its limited resolution. In general, in Punjab, especially in the surrounding areas of Chandigarh, groundwater has been tapped for irrigation and industrial purposes since more than three decades. Irrespective of poor monsoon, ground water is being withdrawn, and the water level is declining that is causing subsidence which is detected clearly from time series analysis of SAR images. We have drawn two major conclusions based on the detailed satellite and ground analysis.

1) Well-known overexploitation of HGS by space geodesy such as GRACE and GRACE-follow-up missions has highly inhomogeneous local structures and mechanisms as shown in the Chandigarh case.
2) The distribution of sediments is involved in the localized patterns of groundwater depletion and consequent on-going ground subsidence.

The pattern of localized ground subsidence centered along an arc shape in the southeastern Chandigarh city area was further investigated by the application of PS and statistical survey. We observed structural instabilities caused by horizontal tilting. It appeared that major architectures as the legendary modern architectures are not very influenced by ground subsidence. However, the continued decline of water level and associated subsidence is a real concern as observed by the instabilities along high vertical subsidence. Technically, this study demonstrates an effective utilization of two complementary time series InSAR techniques based on PS and DS data syncretization. Zooming-up the potential hazard areas by regional observation of GRACE, regional observation of NSBAS, and structural observations of PS, the assessments of risky points were achieved even with public domain medium resolution space geodetic data. The detected structural instability on the cooling system based on the further PS analyses and NSBAS background survey highlighted the potential to extend the approaches identifying localized structural risk with medium resolution InSAR processor. We further suggest that the entities involved could plan to use NASA-Indian Space Research Organisation (ISRO) joint mission (NISAR) data along with in situ data for monitoring of subsidence in the Punjab area.

Acknowledgment

The authors appreciate the sincere discussions with the officers of the Central Ground Water Board, Chandigarh, India. The views presented here are those of the authors. They are also grateful to the anonymous four reviewers for their useful comments/suggestions that have helped us to improve an earlier version of this article.

References

[1] S. K. Mishra, R. P. Singh, and S. Chandra, "Prediction of subsidence in the Indo-gangetic basin carried by groundwater withdrawal," *Eng. Geol.*, vol. 33, no. 3, pp. 227–239, Feb. 1993.

[2] V. M. Tiwari, J. Wahr, and S. Swenson, "Dwindling groundwater resources in northern India, from satellite gravity observations," *Geophys. Res. Lett.*, vol. 36, no. 18, 2009, Art. no. L18401.

[3] R. P. Singh, W. Mehdi, M. Naeimi, A. Sahoo, and R. Kumar, "Analysis of widespread fissures associated with groundwater depletion and extreme rainfall using multi sensor data," in *GRACE, Remote Sensing and Ground-Based Methods in Multi-Scale Hydrology*, vol. 343. Oxfordshire, U.K.: IAHS Press, 2011, pp. 28–33.

[4] F. Cigna and D. Tapete, "Present-day land subsidence rates, surface faulting hazard and risk in Mexico City with 2014–2020 Sentinel-1 IW InSAR," *Remote Sens. Environ.*, vol. 253, Feb. 2021, Art. no. 112161.

[5] T. T. Thoang and P. H. Giao, "Subsurface characterization and prediction of land subsidence for HCM City, Vietnam," *Eng. Geol.*, vol. 199, pp. 107–124, Dec. 2015.

[6] E. Chaussard, F. Amelung, H. Abidin, and S.-H. Hong, "Sinking cities in Indonesia: ALOS PALSAR detects rapid subsidence due to groundwater and gas extraction," *Remote Sens. Environ.*, vol. 128, pp. 150–161, Jan. 2013.

[7] D. Long, B. R. Scanlon, L. Longuevergne, A. Y. Sun, D. N. Fernando, and H. Save, "GRACE satellite monitoring of large depletion in water storage in response to the 2011 drought in Texas," *Geophys. Res. Lett.*, vol. 40, no. 13, pp. 3395–3401, Jul. 2013.

[8] J. S. Famiglietti et al., "Satellites measure recent rates of groundwater depletion in California's Central Valley," *Geophys. Res. Lett.*, vol. 38, no. 3, Feb. 2011, Art. no. L03403.

[9] C. C. Faunt, M. Sneed, J. Traum, and J. T. Brandt, "Water availability and land subsidence in the Central Valley, California, USA," *Hydrogeol. J.*, vol. 24, no. 3, pp. 675–684, May 2016.

[10] J. W. Borchers, "Land subsidence case studies and current research," in *Proc. Dr. Joseph F. Poland Symp. Land Subsidence, 4–5 Oct 1995, Sacramento, California. Special Publication no. 8*. Denver, CO, USA: Association of Engineering Geologists, 1998, pp. 59–71.

[11] M. A. Biot, "General theory of three-dimensional consolidation," *J. Appl. Phys.*, vol. 12, no. 2, pp. 155–164, Feb. 1941.

[12] J. D. Jackson, D. C. Helm, and J. C. Brumley, "The role of poroviscosity in evaluating land subsidence due to groundwater extraction from sedimentary basin sequences," *Geofísica Internacional*, vol. 43, no. 4, pp. 689–695, Oct. 2004.

[13] R. Yamaguchi, "Change of water level of a deep well in the University of Tokyo: Until the end of 1968," *Tokyo Univ. Earthq. Res. Inst. Bull.*, vol. 47, no. 6, pp. 1093–1111, Dec. 1969.

[14] F. Kenselaar and R. Quadvlieg, "Trend-signal modelling of land subsidence," in *Proc. 10th FIG Int. Symp. Deformation Meas.*, 2001, pp. 19–22.

[15] D. L. Galloway and J. Hoffmann, "The application of satellite differential SAR interferometry-derived ground displacements in hydrogeology," *Hydrogeol. J.*, vol. 15, no. 1, pp. 133–154, Jan. 2007.

[16] P. Castellazzi et al., "Land subsidence in major cities of Central Mexico: Interpreting InSAR-derived land subsidence mapping with hydrogeological data," *Int. J. Appl. Earth Observ. Geoinf.*, vol. 47, pp. 102–111, May 2016.

[17] B. Hu, X. Chen, and X. Zhang, "Using multisensor SAR datasets to monitor land subsidence in Los Angeles from 2003 to 2017," *J. Sensors*, vol. 2019, pp. 1–15, Feb. 2019.

[18] B. Osmanoğlu, T. H. Dixon, S. Wdowinski, E. Cabral-Cano, and Y. Jiang, "Mexico City subsidence observed with persistent scatterer InSAR," *Int. J. Appl. Earth Observ. Geoinf.*, vol. 13, no. 1, pp. 1–12, Feb. 2011.

[19] B. Bookhagen, "Himalayan groundwater," *Nature Geosci.*, vol. 5, no. 2, pp. 97–98, Feb. 2012.

[20] M. Shamsudduha and D. K. Panda, "Spatio-temporal changes in terrestrial water storage in the Himalayan river basins and risks to water security in the region: A review," *Int. J. Disaster Risk Reduction*, vol. 35, Apr. 2019, Art. no. 101068.

[21] L. Giosan et al., "Fluvial landscapes of the Harappan civilization," *Proc. Nat. Acad. Sci. USA*, vol. 109, no. 26, pp. E1688–E1694, 2012.

[22] J. Chen, J. Li, Z. Zhang, and S. Ni, "Long-term groundwater variations in Northwest India from satellite gravity measurements," *Global Planet. Change*, vol. 116, pp. 130–138, May 2014.

[23] Y. Fu and J. T. Freymueller, "Seasonal and long-term vertical deformation in the Nepal Himalaya constrained by GPS and GRACE measurements," *J. Geophys. Res., Solid Earth*, vol. 117, no. B3, Mar. 2012, Art. no. B03407.

[24] A. P. Saji et al., "Surface deformation and influence of hydrological mass over Himalaya and North India revealed from a decade of continuous GPS and GRACE observations," *J. Geophys. Res., Earth Surf.*, vol. 125, no. 1, Jan. 2020, Art. no. e2018JF004943.

[25] N. Kadiyan et al., "Assessment of groundwater depletion–induced land subsidence and characterisation of damaging cracks on houses: A case study in Mohali-Chandigarh area, India," *Bull. Eng. Geol. Environ.*, vol. 80, no. 4, pp. 3217–3231, Apr. 2021.

[26] D. K. Sahadevan and A. K. Pandey, "Groundwater over-exploitation driven ground subsidence in the Himalayan Piedmont zone: Implication for aquifer health due to urbanization," *J. Hydrol.*, vol. 617, Feb. 2023, Art. no. 129085.

[27] S. Garg, M. Motagh, J. Indu, and V. Karanam, "Tracking hidden crisis in India's capital from space: Implications of unsustainable groundwater use," *Sci. Rep.*, vol. 12, no. 1, p. 651, Jan. 2022.

[28] A. Gupta, U. Asopa, and R. Bhattacharjee, "Land subsidence monitoring in Jagadhri City using Sentinel 1 data and DInSAR processing," *Multidisciplinary Digit. Publishing Inst.*, vol. 24, no. 1, p. 25, 2019.

[29] A. Ferretti, C. Prati, and F. Rocca, "Permanent scatterers in SAR interferometry," *IEEE Trans. Geosci. Remote Sens.*, vol. 39, no. 1, pp. 8–20, Jan. 2001.

[30] M.-P. Doin et al., "Presentation of the small baseline NSBAS processing chain on a case example: The Etna deformation monitoring from 2003 to 2010 using Envisat data," in *Proc. Fringe Symp. ESA SP*, Frascati, Italy, 2011, pp. 3434–3437.

[31] H. S. Gill et al., "Active transfer faulting in the NW Sub-Himalaya (India) observed by space-borne topographic analyses," *Quaternary Int.*, vol. 585, pp. 15–26, May 2021.

[32] G. Kandpal, B. John, and K. Joshi, "Geotechnical studies in relation to seismic microzonation of Union Territory of Chandigarh," *J. Ind. Geophys. Union*, vol. 13, no. 2, pp. 75–83, 2009.

[33] H. C. Bonsor et al., "Hydrogeological typologies of the Indo-Gangetic basin alluvial aquifer, South Asia," *Hydrogeol. J.*, vol. 25, no. 5, pp. 1377–1406, Aug. 2017.

[34] P. Berardino, G. Fornaro, R. Lanari, and E. Sansosti, "A new algorithm for surface deformation monitoring based on small baseline differential SAR interferograms," *IEEE Trans. Geosci. Remote Sens.*, vol. 40, no. 11, pp. 2375–2383, Nov. 2002.

[35] R. Lanari et al., "An overview of the small baseline subset algorithm: A DInSAR technique for surface deformation analysis," *Pure Appl. Geophsy.*, vol. 164, no. 4, pp. 637–661, Apr. 2007.

[36] P. López-Quiroz, M.-P. Doin, F. Tupin, P. Briole, and J.-M. Nicolas, "Time series analysis of Mexico City subsidence constrained by radar interferometry," *J. Appl. Geophys.*, vol. 69, no. 1, pp. 1–15, Sep. 2009, doi: 10.1016/j.jappgeo.2009.02.006.

[37] W. Gong, A. Thiele, S. Hinz, F. Meyer, A. Hooper, and P. Agram, "Comparison of small baseline interferometric SAR processors for estimating ground deformation," *Remote Sens.*, vol. 8, no. 4, p. 330, Apr. 2016.

[38] G. Nico, R. Tomé, J. Catalão, and P. M. Miranda, "On the use of the WRF model to mitigate tropospheric phase delay effects in SAR interferograms," *IEEE Trans. Geosci. Remote Sens.*, vol. 49, no. 12, pp. 4970–4976, Dec. 2011.

[39] C. Szczypta et al., "Verification of the new ECMWF ERA-interim reanalysis over France," *Hydrol. Earth Syst. Sci.*, vol. 15, no. 2, pp. 647–666, Feb. 2011.

[40] R. Jolivet et al., "Improving InSAR geodesy using global atmospheric models," *J. Geophys. Res., Solid Earth*, vol. 119, no. 3, pp. 2324–2341, Mar. 2014.

[41] J.-R. Kim et al., "Investigation of potential volcanic risk from Mt. Baekdu by DInSAR time series analysis and atmospheric correction," *Remote Sens.*, vol. 9, no. 2, p. 138, Feb. 2017.

[42] J. R. Kim, H. Yun, S. Van Gasselt, and Y. Choi, "Error-regulated multipass DInSAR analysis for landslide risk assessment," *Photogramm. Eng. Remote Sens.*, vol. 84, no. 4, pp. 189–202, Apr. 2018.

[43] M. Lazecký et al., "LiCSAR: An automatic InSAR tool for measuring and monitoring tectonic and volcanic activity," *Remote Sens.*, vol. 12, no. 15, p. 2430, Jul. 2020.

[44] Y. Morishita, M. Lazecky, T. Wright, J. Weiss, J. Elliott, and A. Hooper, "LiCSBAS: An open-source InSAR time series analysis package integrated with the LiCSAR automated Sentinel-1 InSAR processor," *Remote Sens.*, vol. 12, no. 3, p. 424, Jan. 2020.

[45] J. Biggs, T. Wright, Z. Lu, and B. Parsons, "Multi-interferogram method for measuring interseismic deformation: Denali Fault, Alaska," *Geophys. J. Int.*, vol. 170, no. 3, pp. 1165–1179, Sep. 2007.

[46] T. Wang and S. Jonsson, "Phase-Ramp reduction in interseismic interferograms from pixel-offsets," *IEEE J. Sel. Topics Appl. Earth Observ. Remote Sens.*, vol. 7, no. 5, pp. 1709–1718, May 2014.

[47] N. Yagüe-Martínez et al., "Interferometric processing of Sentinel-1 TOPS data," *IEEE Trans. Geosci. Remote Sens.*, vol. 54, no. 4, pp. 2220–2234, Apr. 2016.

[48] N. Yague-Martinez, F. De Zan, and P. Prats-Iraola, "Coregistration of interferometric stacks of Sentinel-1 TOPS data," *IEEE Geosci. Remote Sens. Lett.*, vol. 14, no. 7, pp. 1002–1006, Jul. 2017.

[49] A. Ferretti, A. Fumagalli, F. Novali, C. Prati, F. Rocca, and A. Rucci, "A new algorithm for processing interferometric data-stacks: SqueeSAR," *IEEE Trans. Geosci. Remote Sens.*, vol. 49, no. 9, pp. 3460–3470, Sep. 2011.

[50] S. Mirzaee, F. Amelung, and H. Fattahi, "Non-linear phase linking using joined distributed and persistent scatterers," *Comput. Geosci.*, vol. 171, Feb. 2023, Art. no. 105291.

[51] D. Perissin and F. Rocca, "High-accuracy urban DEM using permanent scatterers," *IEEE Trans. Geosci. Remote Sens.*, vol. 44, no. 11, pp. 3338–3347, Nov. 2006.

[52] A. Ferretti, C. Prati, and F. Rocca, "Nonlinear subsidence rate estimation using permanent scatterers in differential SAR interferometry," *IEEE Trans. Geosci. Remote Sens.*, vol. 38, no. 5, pp. 2202–2212, 2000.

[53] T. Fuhrmann and M. C. Garthwaite, "Resolving three-dimensional surface motion with InSAR: Constraints from multi-geometry data fusion," *Remote Sens.*, vol. 11, no. 3, p. 241, Jan. 2019.

[54] Y. Fialko, M. Simons, and D. Agnew, "The complete (3-D) surface displacement field in the epicentral area of the 1999 M_W7.1 Hector Mine Earthquake, California, from space geodetic observations," *Geophys. Res. Lett.*, vol. 28, no. 16, pp. 3063–3066, Aug. 2001.

[55] H.-W. Yun, J.-R. Kim, H. Yoon, Y. Choi, and J. Yu, "Seismic surface deformation risks in industrial hubs: A case study from Ulsan, Korea, using DInSAR time series analysis," *Remote Sens.*, vol. 11, no. 10, p. 1199, May 2019.

[56] R. Torres et al., "GMES Sentinel-1 mission," *Remote Sens. Environ.*, vol. 120, pp. 9–24, May 2012.

[57] D. S. Pai, M. Rajeevan, O. P. Sreejith, B. Mukhopadhyay, and N. S. Satbha, "Development of a new high spatial resolution (0.25° × 0.25°) long period (1901–2010) daily gridded rainfall data set over India and its comparison with existing data sets over the region," *Mausam*, vol. 65, no. 1, pp. 1–18, Jan. 2014.

[58] T. H. Syed, J. S. Famiglietti, M. Rodell, J. Chen, and C. R. Wilson, "Analysis of terrestrial water storage changes from GRACE and GLDAS," *Water Resour. Res.*, vol. 44, no. 2, Feb. 2008, Art. no. W02433.

[59] P. Castellazzi, L. Longuevergne, R. Martel, A. Rivera, C. Brouard, and E. Chaussard, "Quantitative mapping of groundwater depletion at the water management scale using a combined GRACE/InSAR approach," *Remote Sens. Environ.*, vol. 205, pp. 408–418, Feb. 2018.

[60] B. Vishwakarma, B. Devaraju, and N. Sneeuw, "What is the spatial resolution of grace satellite products for hydrology?" *Remote Sens.*, vol. 10, no. 6, p. 852, May 2018.
[61] C. Robert, C. William, and T. Irma, "STL: A seasonal-trend decomposition procedure based on loess," *J. Off. Statist.*, vol. 6, no. 1, pp. 3–73, 1990.
[62] S. K. Joshi et al., "Tracing groundwater recharge sources in the northwestern Indian alluvial aquifer using water isotopes (δ18O, δ2H and 3H)," *J. Hydrol.*, vol. 559, pp. 835–847, Apr. 2018, doi: 10.1016/j.jhydrol.2018.02.056.
[63] *CGWB 2013*, SAS Nagar District, Central Ground Water Board, NW Region, Chandigarh, India, 2013.
[64] Y. Cao, Y.-N. Wei, W. Fan, M. Peng, and L. Bao, "Experimental study of land subsidence in response to groundwater withdrawal and recharge in Changping District of Beijing," *PLoS ONE*, vol. 15, no. 5, May 2020, Art. no. e0232828.
[65] K. Sushanth, A. Bhardwaj, D. Loshali, and B. Pateriya, "Temporal land-use change analysis of Patiala-Ki-Rao watershed in Shivalik Foot-Hills using Remote Sensing and GIS," *J. Agricult. Eng.*, vol. 55, no. 4, pp. 57–65, 2019.
[66] S. Kumar Joshi et al., "Strongly heterogeneous patterns of groundwater depletion in Northwestern India," *J. Hydrol.*, vol. 598, Jul. 2021, Art. no. 126492.
[67] C.-T. Chen, J.-C. Hu, C.-Y. Lu, J.-C. Lee, and Y.-C. Chan, "Thirty-year land elevation change from subsidence to uplift following the termination of groundwater pumping and its geological implications in the Metropolitan Taipei Basin, Northern Taiwan," *Eng. Geol.*, vol. 95, nos. 1–2, pp. 30–47, Nov. 2007.
[68] W. R. Neely, A. A. Borsa, J. A. Burney, M. C. Levy, F. Silverii, and M. Sneed, "Characterization of groundwater recharge and flow in California's San Joaquin Valley from InSAR-observed surface deformation," *Water Resour. Res.*, vol. 57, no. 4, Apr. 2021.
[69] Q. Yang et al., "Multi-scale analysis of the relationship between land subsidence and buildings: A case study in an eastern Beijing Urban Area using the PS-InSAR technique," *Remote Sens.*, vol. 10, no. 7, p. 1006, Jun. 2018.
[70] X. Qin, M. Liao, L. Zhang, and M. Yang, "Structural health and stability assessment of high-speed railways via thermal dilation mapping with time-series InSAR analysis," *IEEE J. Sel. Topics Appl. Earth Observ. Remote Sens.*, vol. 10, no. 6, pp. 2999–3010, Jun. 2017.
[71] J. K. Ord and A. Getis, "Local spatial autocorrelation statistics: Distributional issues and an application," *Geographical Anal.*, vol. 27, no. 4, pp. 286–306, Sep. 2010.
[72] K. H. Hamed, "Exact distribution of the Mann–Kendall trend test statistic for persistent data," *J. Hydrol.*, vol. 365, nos. 1–2, pp. 86–94, Feb. 2009.
[73] C. He, P. Shi, D. Xie, and Y. Zhao, "Improving the normalized difference built-up index to map urban built-up areas using a semiautomatic segmentation approach," *Remote Sens. Lett.*, vol. 1, no. 4, pp. 213–221, Dec. 2010.
[74] J. P. Stewart, G. L. Fenves, and R. B. Seed, "Seismic soil-structure interaction in buildings. I: Analytical methods," *J. Geotech. Geoenvironmental Eng.*, vol. 125, no. 1, pp. 26–37, Jan. 1999.
[75] B. Dzegniuk, R. Hejmanowski, and A. Sroka, "Evaluation of the damage hazard to building objects on the mining areas considering the deformation course in time," in *Proc. 10th Int. Congr. Int. Soc. Mine Surveying*, 1997, pp. 2–6.
[76] M. G. Mustafin, V. A. Valkov, and A. I. Kazantsev, "Monitoring of deformation processes in buildings and structures in metropolises," *Proc. Eng.*, vol. 189, pp. 729–736, Jan. 2017.
[77] H. Fattahi and F. Amelung, "DEM error correction in InSAR time series," *IEEE Trans. Geosci. Remote Sens.*, vol. 51, no. 7, pp. 4249–4259, Jul. 2013.
[78] J. Jung, D.-J. Kim, S. K. P. Vadivel, and S.-H. Yun, "Long-term deflection monitoring for bridges using X and C-band time-series SAR interferometry," *Remote Sens.*, vol. 11, no. 11, p. 1258, May 2019.
[79] Y. Yan et al., "Mexico City subsidence measured by InSAR time series: Joint analysis using PS and SBAS approaches," *IEEE J. Sel. Topics Appl. Earth Observ. Remote Sens.*, vol. 5, no. 4, pp. 1312–1326, Aug. 2012.
[80] G.-Y. Wang et al., "Land subsidence and uplift related to groundwater extraction in Wuxi, China," *Quart. J. Eng. Geol. Hydrogeol.*, vol. 53, no. 4, pp. 609–619, Nov. 2020.
[81] N. Phien-wej, P. H. Giao, and P. Nutalaya, "Field experiment of artificial recharge through a well with reference to land subsidence control," *Eng. Geol.*, vol. 50, nos. 1–2, pp. 187–201, Sep. 1998.

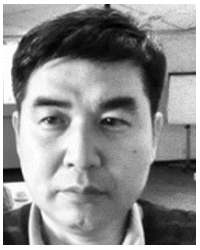

Jungrack Kim received the B.Sc. and M.Sc. degrees from Yonsei University, Seoul, South Korea in 1989 and 1992, respectively, the B.Eng. degree from Soogang University, Seoul, in 1997, and the Ph.D. degree from the University College London (UCL), London, U.K., in 2007.

He was a Research Fellow with the UCL Mullard Space Science Laboratory, Dorking, U.K., and a Research Professor with the University of Seoul, Seoul. He is currently a Head Research Scientist with Future Vision Inc., Icheon, Republic of Korea. He has been studying extraterrestrial/terrestrial topographies and their migrations using various remote sensing techniques like stereo images, interferometric synthetic aperture radar (InSAR), LiDAR, and multispectral sensors. His recent studies focus on erosion/deformation tracing on Earth and planetary bodies and machine-learning applications for topographical datasets. In those areas, he has authored or coauthored more than 50 scientific articles.

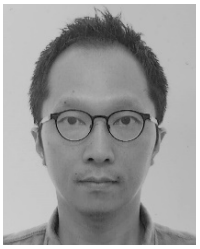

Shih-Yuan Lin received the Ph.D. degree from the School of Civil Engineering and Geosciences, Newcastle University, Newcastle upon Tyne, U.K., in 2007.

He was a Post-Doctoral Researcher with the UCL Mullard Space Science Laboratory, Dorking, U.K. He is currently an Associate Professor with National Chengchi University, Taipei City, Taiwan. His research topics cover photogrammetric, laser scanning, and interferometric synthetic aperture radar (InSAR) processing and analyses. He is also committed to integrating the geomatics technology in the social sciences applications, such as geohazard risk assessment over indigenous settlements based on time series InSAR and local knowledge, remote sensing estimation of building deformation, and evaluation of driving factors. He has authored or coauthored more than 30 academic articles in these research fields.

Tejpal Singh received the M.Sc. (Hons.) and Ph.D. degrees from Panjab University, Chandigarh, India, in 2000 and 2006, respectively.

Subsequently, he worked at the Indian Institute of Technology Roorkee, Roorkee, India, as a Post-Doctoral Fellow. He worked as a Scientist at the CSIR-Centre for Mathematical Modelling and Computer Simulation (now CSIR-4PI), Bengaluru, India. He is currently a Senior Scientist with the CSIR-Central Scientific Instruments Organisation, Chandigarh. His research works include tectonic geomorphology, geology of earthquakes and active faults, seismotectonic, seismic hazard, and geometric/mathematical modeling of surface deformation and geological features. He has edited three journal special issues related to current advances in *Surface Deformation*, and also he has more than 30 research publications.

Ramesh P. Singh (Senior Member, IEEE) received the B.S., M.Sc., and Ph.D. degrees from Banaras Hindu University, Varanasi, India, in 1974, 1976, and 1980, respectively.

He was a Professor with the Indian Institute of Technology Kanpur, Kanpur, India, from 1986 to 2007; and with George Mason University, Fairfax, VA, USA, from 2003 to 2005 and from 2007 to 2009. He is currently a Professor with the Schmid College of Science and Technology, Chapman University, Orange, CA, USA. He has authored more than 200 articles. His research interests include natural hazards, early warning of coastal earthquakes, soil moisture, landslides, snow avalanches, floods, dust storms, remote sensing applications, geophysical exploration, atmospheric pollution, and mining environment.

Dr. Singh is the Chief Editor of the *Geomatics*, *Natural Hazards,* and *Risk* (Taylor & Francis, U.K.).